Compartmentalization of the Outer Hair Cell Demonstrated by Slow Diffusion in the Extracisternal Space

Olga Gliko,[†] Peter Saggau,[‡§] and William E. Brownell[†‡§*]
[†]Department of Otorhinolaryngology-Head and Neck Surgery, and [‡]Department of Neuroscience, Baylor College of Medicine, Houston, Texas; and [§]Department of Bioengineering, Rice University, Houston, Texas

ABSTRACT In the outer hair cell (OHC), the extracisternal space (ECiS) is a conduit and reservoir of the molecular and ionic substrates of the lateral wall, including those necessary for electromotility. To determine the mechanisms through which molecules are transported in the ECiS of the OHC, we selectively imaged the time-dependent spatial distribution of fluorescent molecules in a <100 nm layer near the cell/glass interface of the recording chamber after their photolytic activation in a diffraction-limited volume. The effective diffusion coefficient was calculated using the analytical solution of the diffusion equation. It was found that diffusion in the ECiS is isotropic and not affected by depolarizing the OHC. Compared with free solution, the diffusion of 10 kDa dextran was slowed down in both the ECiS and the axial core by a factor of 4.6 and 1.6, respectively.

INTRODUCTION

Outer hair cells (OHCs) play an important role in cochlea amplification (1–3). The OHC lateral wall is ~100 nm thick and consists of two axially concentric cylindrical layers—the plasma membrane (PM) and subsurface cisterna (SSC)—separated by the extracisternal space (ECiS) (Fig. 1). The ECiS is 20–40 nm thick and filled with fluid, and contains a cytoskeletal network called the cortical lattice (CL). The CL consists of circumferentially oriented actin filaments that are spaced by ~40 nm and interconnected by longitudinally oriented spectrin. Radially oriented pillars of unknown composition connect the parallel actin filaments to the PM. The tensile properties of the CL together with cytoplasmic turgor pressure allow the OHC to maintain its cylindrical shape and to generate electromechanical forces required for hearing (4). The ECiS serves as a reservoir and a conduit for ions, water, and other molecular species, including anions necessary for electromotility. Its transport properties for species other than water remain unknown. Estimations of the water permeability of the ECiS have shown that the resistance to water transport is limited by the hydraulic resistance of the PM, i.e., the hydraulic permeability of the PM is much smaller than that of the ECiS (5). To the best of our knowledge, no experimental data on molecular transport in the ECiS have been provided. Because of the size and structure of the ECiS, novel experimental methods are needed to probe its transport properties and investigate diffusive and convective transport of neutral and charged fluorescently labeled molecules. In vivo and in vitro studies of simultaneous diffusion and convection using fluorescently labeled markers have been conducted in the past using fluorescence recovery after photobleaching (FRAP) (6,7), but not at the scale of the ECiS. The disadvantages of FRAP that make it unsuitable for our study are its relative slowness, as well as a low signal/noise ratio as a result of measuring a low-intensity signal in the presence of a high-intensity background. Another drawback of FRAP is that it results in reversible photobleaching, a phenomenon that is not well understood but is attributed to a spontaneous and radical-induced recovery from the triplet state (8).

The combination of two techniques has rendered possible a novel experimental approach for studying transport phenomena in nanostructures. These techniques are microphotolysis of caged fluorescent compounds and total internal reflection fluorescence microscopy (TIRFM). Microphotolysis has become a powerful tool to rapidly ''deliver'' substances to small volumes, since inert molecules can readily be put in place and activated with a flash of light within milliseconds (9,10). With TIRFM, the fluorophore excitation volume can be limited to a thin layer of tens to hundreds of nanometers (11,12).

In this work, we combined these two techniques to instantaneously and selectively deliver tagged fluorescent molecules to a small volume inside the cell and to image their fate in nanostructures such as the ECiS with a selective wide-field imaging scheme. We used the diffusion equation to analyze the experimental data and obtain quantitative transport characteristics of the ECiS.

MATERIALS AND METHODS

OHC isolation

Albino guinea pigs of either sex weighing 200–300 g were anesthetized and decapitated according to the Baylor College of Medicine's guidelines for the use of laboratory animals. The temporal bones were removed, and the organ

Submitted April 9, 2009, and accepted for publication June 2, 2009.

*Correspondence: brownell@bcm.edu

Editor: Levi A. Gheber.

0006-3495/09/08/1215/10 $2.00

doi: 10.1016/j.bpj.2009.06.011

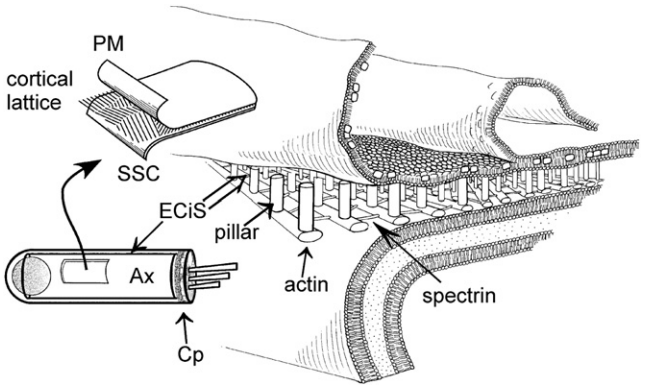

FIGURE 1 OHC lateral wall is ~100 nm thick and consists of the plasma membrane (PM), the cortical lattice (CL), and the subsurface cisterna (SSC). The CL is composed of microdomains of parallel actin filaments cross-linked by spectrin. Pillars link actin filaments to the PM. The axial core (Ax) is the center of the OHC, and the extracisternal space (ECiS) is the fluid-filled space between the PM and the SSC, wherein lies the CL. The stereocilia are rooted in the cuticular plate (Cp) (3).

of Corti was isolated from the cochlea and incubated in trypsin (1 mg/mL; Sigma, St. Louis, MO) for ~5 min. Gentle pipetting was performed to dissociate the OHCs before transferring them to a glass-bottom petri dish that was polylysine-coated by the manufacturer (MatTek, Ashland, MA) to enhance cell attachment. Dissection and experiments were performed in an extracellular solution containing (in mM) 100 NaCl, 20 CsCl, 20 *N*-$(CH_2CH_3)_4Cl$, 10 HEPES, 2 $CoCl_2$, 1.47 $MgCl_2$, 2 $CaCl_2$. The internal solution of the whole-cell pipette contained (in mM) 140 CsCl, 2 $MgCl_2$, 10 EGTA, and 10 HEPES. The pH was 7.2 ± 0.02 and the osmolarity was 300 ± 2 mOsm/kg. We used the OHCs with lengths of 60–90 μm. All OHCs were used within 4 h after the animal was killed, and had a uniformly cylindrical shape without swelling, no Brownian motion in the cytoplasm, and a basally located nucleus.

Whole-cell voltage clamping

Patch pipettes with a typical resistance of 3–4 MΩ were pulled from quartz capillary tubes (Sutter Instrument, Novato, CA) with a CO_2 laser-based micropipette puller (Sutter Instrument). An Axopatch 200B amplifier (Axon Instruments, Foster City, CA) was used for recordings. Electrical seals (>1 GΩ) were formed between the pipette and cell membrane at the basal end of the OHC to ensure the integrity of the lateral wall structure. After the pipette capacitance was compensated, gentle suction was applied to establish a whole-cell configuration, and the holding potential was set to −60 mV. The holding potential was changed to 0 and +60 mV for several seconds during some of the experiments. Custom computer software written in LabVIEW (National Instruments, Austin, TX) controlled the experiment and data acquisition.

Optical setup

To determine the mechanisms of molecular transport in the ECiS, we imaged the fate of intracellularly delivered molecules conjugated with caged, initially nonfluorescent molecules, which upon ultraviolet (UV) irradiation were photolyzed and became fluorescent. The diffusion indicator, DMNB-caged fluorescein dextran (10 kDa, anionic; Invitrogen, Carlsbad, CA), was added to the internal solution (100 μM final concentration) and loaded into the OHC by patch pipette. In OHCs, imaging of fluorescent molecules is complicated by the small radial dimension of the ECiS (~20–40 nm thickness) and the fact that the axial core (AX), which is in close proximity (~100 nm distance), is also filled with the caged compound. Therefore, measures have to be taken to limit the photolysis or to restrict the fluorescence imaging to the ECiS.

To image transport in the ECiS, we photolyzed the caged fluorophore within both the ECiS and the AX, but we imaged fluorescence from the ECiS only by using total internal reflection (TIR) excitation (Fig. 2 *a*). In TIR, a thin evanescent field decaying exponentially in the axial direction excites fluorophores near an interface where the refractive index steps down, e.g., a glass/water interface. Using a 1.45 NA objective lens, the smallest penetration depth of the excitation field, achieved at the largest angle of $\theta = 72.8°$, is 67 nm (1/e criterion). Our experimental setup combining UV microphotolysis and TIRFM using visible light is shown in Fig. 2 *b*. Two lasers were used: a pulsed, diode-pumped solid-state Q-switched UV laser (3500; DPSS Lasers, Santa Clara, CA) with 355 nm wavelength and 50 kHz repetition rate, and a continuous-wave Ar-laser (488 nm; Omnichrome 532-AP-A01; Melles Griot, Carlsbad, CA). The laser beams were attenuated, expanded, and coupled through the back port of a standard inverted microscope into an oil immersion 100× objective lens with NA of 1.45 (Carl Zeiss, Gottingen, Germany). The inverted microscope (Axiovert S100TV; Carl Zeiss) with its bottom port for direct fluorescence access allowed us to perform optical measurements and patch-clamping recordings simultaneously. A petri dish with isolated OHCs was placed onto the translational stage of the microscope, which supported convenient electrophysiological recording and media replacement. The pipette holder was mounted on the translational stage, which allowed us to adjust the position of the whole-cell patched OHC relative to the laser beams. The UV beam was expanded to fill the back focal aperture of the objective lens, resulting in a focus with a diameter of 1.4 μm in the center of the object

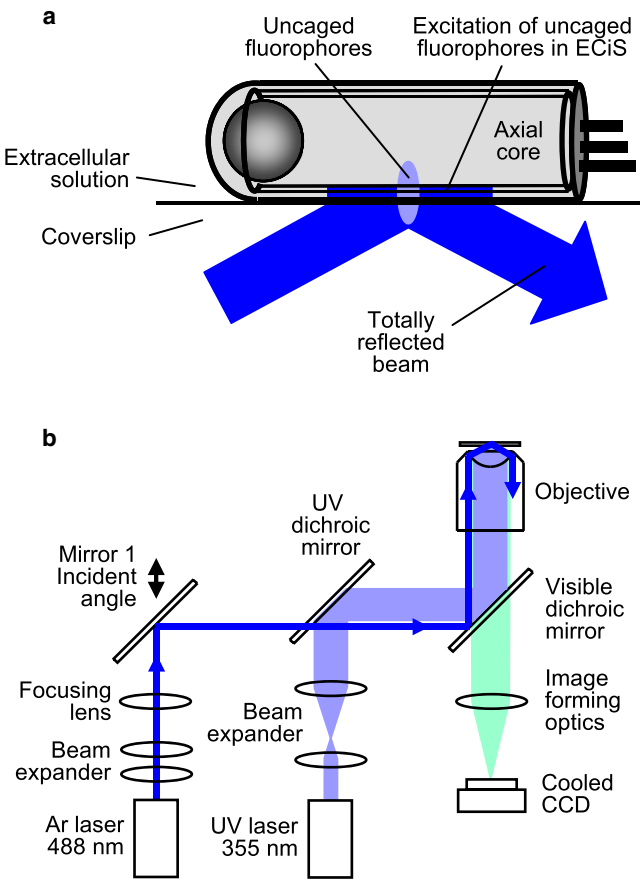

FIGURE 2 (*a*) UV photolysis activation of fluorescent dye in a diffraction-limited volume inside the OHC followed by selective TIR fluorescence excitation in the ECiS. (*b*) Experimental setup for measuring transport in the OHC.

plane. The expanded visible beam was focused at the back focal aperture, providing a collimated beam with a diameter of 30 μm in the object plane. The incident angle of the visible beam was adjusted by mechanical translation of a mirror (Fig. 2 *b*). This allowed us to change the penetration depth of the evanescent excitation for TIRF imaging, and switch to epifluorescence imaging by setting the incident angle below the critical one ($\theta = 61.2^\circ$).

The fluorescence emitted by the cell was collected by the same objective lens and passed through the dichroic mirror and the additional long-pass filter (not shown) to block residual excitation light. The mirror assembly (not shown) attached to the microscope bottom port directed the light collected by the objective lens to a cooled CCD camera (CH250/A; Photometrics, Tucson, AZ), which was used to capture fluorescence images.

Fluorescence measurements

For measurements of transport in the OHC, the whole-cell patch clamp was established and the cell was filled with the caged dye. In addition to the caged fluorescein, the internal pipette solution contained a low concentration (<10 μM) of fluorescein (Sigma, St. Louis, MO). The OHC was illuminated with TIR light, and the surface part of the cell adjacent to the glass coverslip became fluorescent due to emission from the low amount of free fluorescein. The OHC fluorescent area was brought to focus and moved laterally, such that the UV beam would be centered in the area during the photolysis. Photolysis was always induced well away from the OHC nucleus. Alternatively, epi-illumination was used to measure transport in the AX for comparison with the ECiS. The caged fluorophore was photolyzed by exposure to the focused UV beam for 10 ms. The exposure time was computer-controlled by utilizing the external Q-switch mode of the laser. The fluorescence was excited continuously with the TIR beam during the uncaging and subsequent measurement periods. A sequence of images was taken with an exposure time of 10–14 ms and a total time of 4–5 s. Image acquisition and UV exposure were synchronized using custom software (LabVIEW), such that data acquisition started before photolysis and continued until uniform distribution of the uncaged fluorophore was reached. The images were corrected using MATLAB software (The MathWorks, Natick, MA) by subtracting a frame acquired before UV exposure to remove the background fluorescence from uncaged dye before photolysis. The resulting images were subsequently normalized using the same frame to remove nonuniformities of fluorescence due to inhomogeneous intensity of the visible excitation beam. This also eliminated the effect of a nonuniform distance between the cell surface and coverslip. Several tests, including measurements in free solution, were done to ensure proper data processing. For each cell, uncaging was repeated several times, and at the end of each experiment photolyzed dye was distributed uniformly. For measurements in free solution, a 20 μm layer of internal solution containing DMNB-caged fluorescein dextran (10 kDa, 100 μM) was sandwiched between two glass coverslips. All experiments in OHCs and free fluorescein solution were carried at a room temperature of 22°C.

Determination of effective diffusivity

Sequences of corrected images were used to determine the nature of the molecular transport and to calculate the effective diffusivity. Assuming a linear dependence of fluorescence on excitation intensity, the fluorescence intensity is proportional to the concentration of the uncaged dye. As a result of photolysis, a fraction of caged dye molecules became photolyzed rapidly in a small volume inside the OHC. The initial distribution of uncaged fluorescent dye corresponded to the intensity pattern of a focused UV beam, which can be approximated as a three-dimensional (3D) Gaussian distribution. The time evolution of the uncaged dye concentration $C(x,y,z,t)$ is described by the diffusion-convection equation:

$$\frac{\partial C}{\partial t} + \mathbf{u}\nabla C = D\left(\nabla^2 C + \frac{FZC}{RT}\nabla^2\psi\right), \qquad (1)$$

where $\mathbf{u}$ is the fluid velocity, D is the effective diffusion coefficient, F is the Faraday constant, Z is the ionic charge, R is the universal gas constant, and ψ is the electric potential. By measuring the time evolution of the spatial distribution of the fluorescence intensity, including the spreading of the fluorescence spot as a result of diffusion and the drift of the spot centroid, it is possible to calculate both the effective diffusion coefficients and the fluid velocity for fluorescently labeled molecules. Equation 1 can be solved numerically to yield the concentration distribution as a function of time after photolysis. The results of computations can be fit to the experimental data to determine the effective diffusion coefficient and the fluid velocity.

In the absence of convection and electric field, the molecular transport is determined by diffusion:

$$\frac{\partial C}{\partial t} = D_x\frac{\partial^2 C}{\partial x^2} + D_y\frac{\partial^2 C}{\partial y^2} + D_z\frac{\partial^2 C}{\partial z^2}, \qquad (2)$$

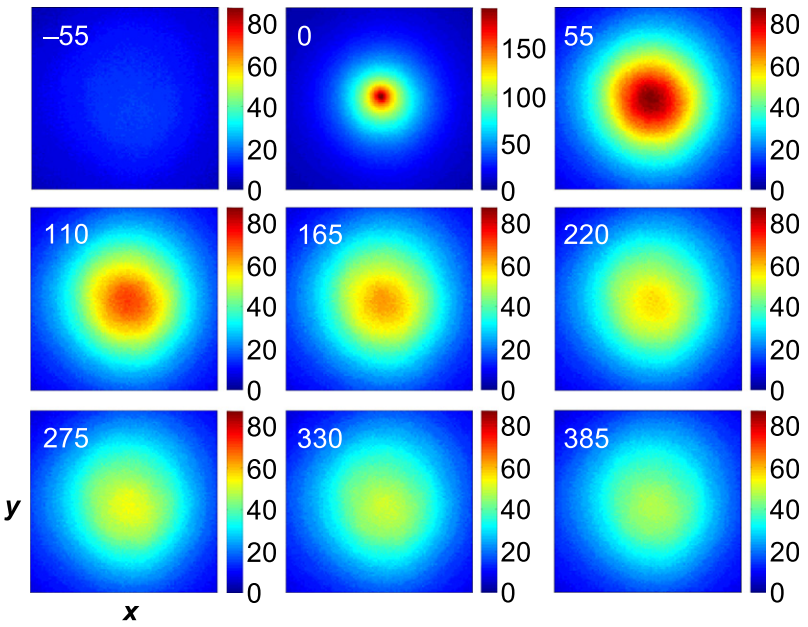

FIGURE 3 Epifluorescence images of the spatiotemporal distribution of uncaged fluorescein-dextran in free solution. Image size was 23 × 23 μm^2. The images are labeled in milliseconds as measured from the uncaging event.

where D_x, D_y, D_z are the effective diffusion coefficients in the x, y, and z directions, respectively. Here, Eq. 2 is generalized to the case of anisotropic diffusion. Since the initial distribution of uncaged dye is a 3D Gaussian, a simple analytical solution can be used to determine the effective diffusion coefficients:

$$C(x,y,z,t) = \frac{1}{(4\pi)^{3/2}} \frac{1}{\sqrt{D_x D_y D_z}} \frac{1}{\sqrt{(t+a)(t+b)(t+c)}} \times \exp\left[-\frac{(x-x')^2}{4D_x(t+a)} - \frac{(y-y')^2}{4D_y(t+b)} - \frac{(z-z')^2}{4D_z(t+c)} \right]. \quad (3)$$

The parameters a, b, and c in Eq. 3 are chosen depending on the actual dimensions of the photolyzing focused UV beam. The analytical solution (Eq. 3) is valid for the 3D Gaussian source spreading in an infinite medium. It is a good approximation in the case of diffusion in free solution, as well as in the AX of the OHC. In this case, diffusion in each dimension is intrinsically independent of the two other dimensions. Since the experimentally measured data were two-dimensional (2D), the data analysis was simplified to 2D diffusion. The x- and y- intensity profiles through the maximum of the fluorescence image at each time were fitted to a Gaussian, and the square of the width at 1/e of the maximum was plotted as a function of time: $(\Delta x)^2 = 16D_x t$, $(\Delta y)^2 = 16D_y t$. The slope of the plot provided the diffusivity values, D_x or D_y. The slope was calculated by the least-square method, and Student's t-test was used to compare averages. The geometry of the UV laser uncaging spot was such that the axial size was ~3 times larger than the lateral, and thus larger by a factor of ~100 than the thickness of the ECiS. Therefore, the uncaging beam diameter was assumed to be uniform through the entire thickness of the ECiS. With such beam geometry, the axial concentration gradient of uncaged fluorescein across the ECiS is negligible. As a result, the contribution of the diffusion in the z direction was ignored, and a 2D analysis was performed.

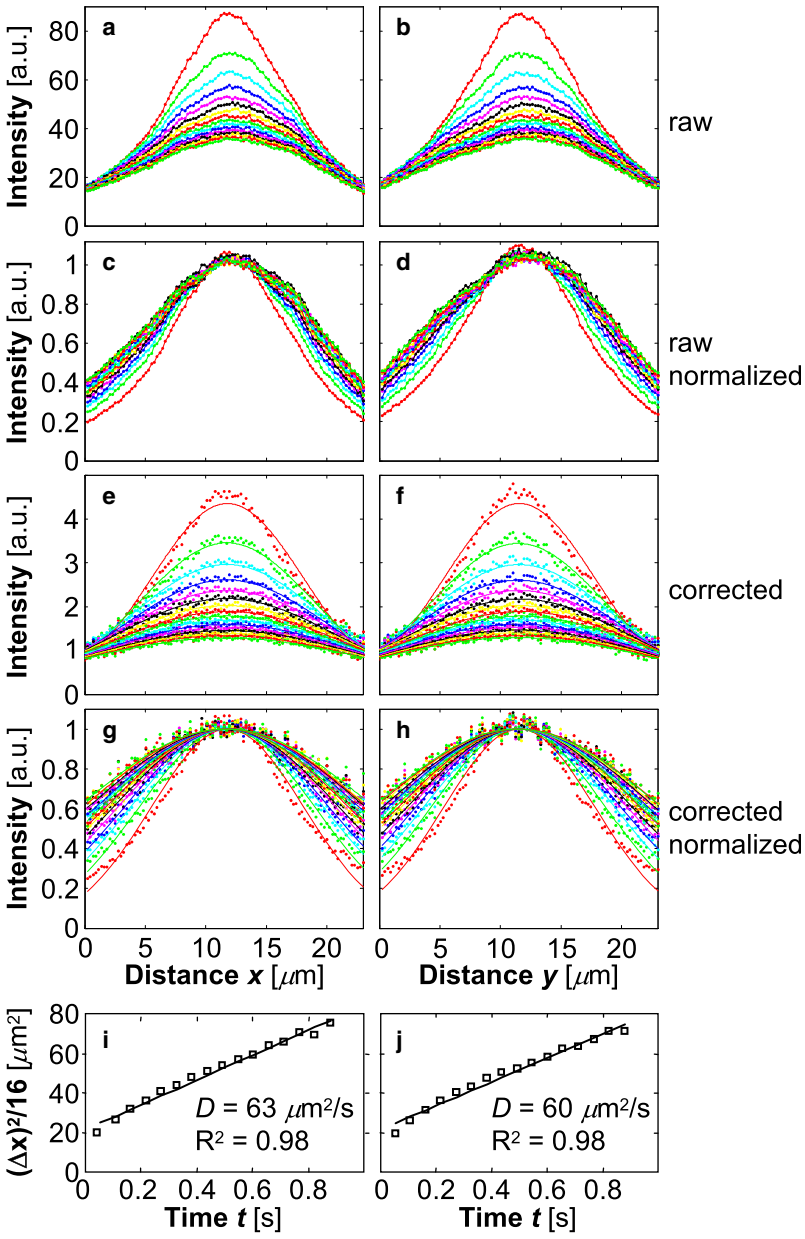

FIGURE 4 Determination of the effective diffusivity of uncaged fluorescein-dextran in free solution. (*a* and *b*) x- and y-Intensity profiles through the center of the images shown in Fig. 3. (*c* and *d*) Normalized profiles of *a* and *b*. (*e* and *f*) Corrected profiles of *a* and *b* (*dots*) were fit by Gaussian distributions (*solid lines*). (*g* and *h*) Normalized profiles of *e* and *f*. (*i* and *j*) Squared widths of Gaussian profiles were plotted as a function of time. The slope of the line calculated by the least-square method is the effective diffusivity.

RESULTS

Diffusion in free solution

For these experiments, uncaged fluorophores were allowed to diffuse freely in a 20 μm thick layer of internal solution in the absence of convection or electric field. When low-molecular-weight caged fluorescein was uncaged in free solution (and in the OHC as well), the diffusional spread of the initial dye distribution occurred too rapidly for useful quantitative information to be obtained from the acquired images. Therefore, a significantly larger molecule, DMNB-caged fluorescein dextran (10 kDa, 100 μM), was used. Fig. 3 shows an acquired sequence of images of the spatio-temporal distribution of fluorescein dextran after uncaging. The image size was 23 $\times$ 23 μm^2, image acquisition rate was 18 frames/s, and total imaging time was 4 s. The first image ($-$55 ms; Fig. 3) was taken just before the photolysis event. The second image (0 ms; Fig. 3) represents the initial distribution of uncaged dye taken at the time of UV photolysis. Subsequent images (only a few are shown in Fig. 3) represent the evolution of the initially uncaged dye. Orthogonal intensity profiles were determined through the center of the fluorescence distribution for each image (Fig. 4, *a* and *b*, respectively). The maximum intensity decreases and the profile width increases with time. The widening is more clearly seen when intensity distributions are normalized to their maximum value (Fig. 4, *c* and *b*). The absence of any displacement of the centroid indicates pure diffusion in the absence of convection. Thus, the analytical solution (Eq. 3) of the diffusion equation (Eq. 2) was applied to determine the effective diffusion coefficient. As described in Materials and Methods, the images were corrected to eliminate any nonuniformity of excitation intensity. The corrected profiles corresponding to Fig. 4, *a–d* are shown in Fig. 4, *e–h*. The profile at each point in time was fit by a Gaussian (*solid lines* in Fig. 4, *e–h*). Squared widths of Gaussians were plotted as a function of time (Fig. 4, *i* and *j*). The slopes of the plots (Fig. 4, *i* and *j*) were calculated by the least-square method, providing the same value for *x* and *y* directions. Employing TIR illumination instead of epi-illumination did not affect the measured diffusivity values. The averaged value of the measured effective diffusion coefficient in free solution, D_{free}, was 65 $\pm$ 10 $\mu m^2/s$ ($n = 5$), which agreed well with a previously reported value of 68 $\pm$ 11 $\mu m^2/s$ for a temperature of 22°C (13). The fact that the diffusion was the same in bulk solution as it was at the surface provides further justification for 2D analysis of diffusion in the ECiS.

Transport in the OHC

After diffusivity measurements were validated for the case of free solution, we carried out experiments in OHCs. TIR illumination of OHCs loaded with fluorescein resulted in fluorescence in an area that sometimes extended from the base to the apical end of the cell and had a width of ~4–7 μm. The width was significantly larger than the expected value of ~2 μm, which was estimated by taking into account the cylindrical shape of the OHC with a diameter of ~9 μm and the penetration depth of TIR illumination of $<$100 nm. To validate the correct limitation of the excitation depth in

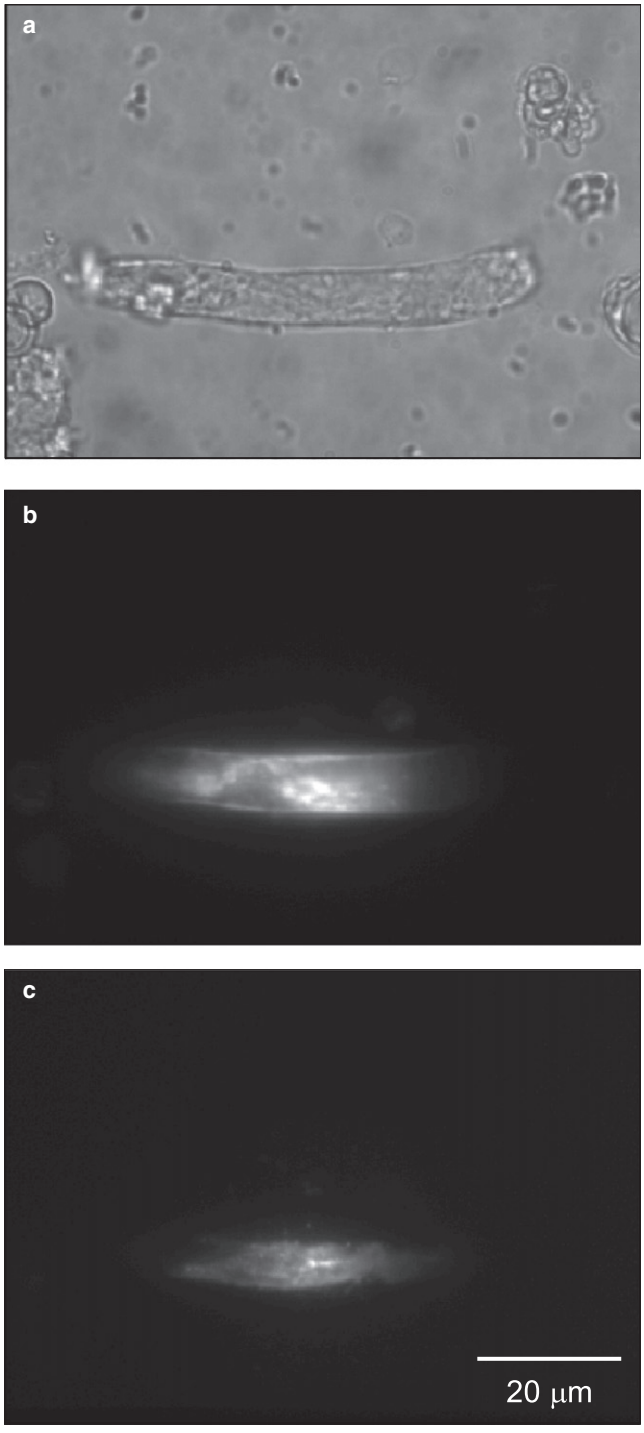

FIGURE 5 Testing contact area of the OHC with polylysine-coated glass coverslip. The PM of the OHC was stained with Di-8-ANEPPS. (*a*) Bright-field image of the OHC. (*b*) Epifluorescence image of the OHC. (*c*) TIRFM image of the OHC shows cell-glass contact area.

the OHC, we tested the cell/glass contact area by labeling the OHC's PM with Di-8-ANEPPS (Invitrogen). The dye was added to a petri dish with isolated cells (100 μM final concentration) and washed away after a 15-min incubation. A comparison between epifluorescence and TIRFM images of the cell, as well as a bright-field image, is shown in Fig. 5. With epi-illumination, the entire PM of the cell was fluorescent (Fig. 5 *b*). With TIR illumination, fluorescence was only excited in the part of the cell PM that was in contact with the coverslip and therefore located within a <100 nm distance from it. The width of the contact area shown in Fig. 5 *c* was ~6 μm. This was typical for most of the OHCs when polylysine-coated glass was used. The increased contact area indicates flattening of the cell lateral wall where it was in contact with the coverslip.

During the experiments, we minimized the penetration depth of the TIR illumination by using the largest incident angle achievable with the employed objective lens, which was assumed to be <100 nm (the theoretical minimum is 67 nm for NA 1.45). Though the thickness of the ECiS is unknown, estimations based on electron microscopy imaging give values of 20–40 nm. Together with the PM and SSC, the total thickness of the lateral wall is ~100 nm. Taking into account an exponential decrease of excitation intensity with distance from the coverslip in TIRF, it is fair to assume that the uncaged molecules in the AX are not excited efficiently, and measured fluorescence is dominated by uncaged molecules located in the ECiS.

Fig. 6 illustrates a typical experiment in the OHC. The cell was held at −60 mV and photolysis was induced well away

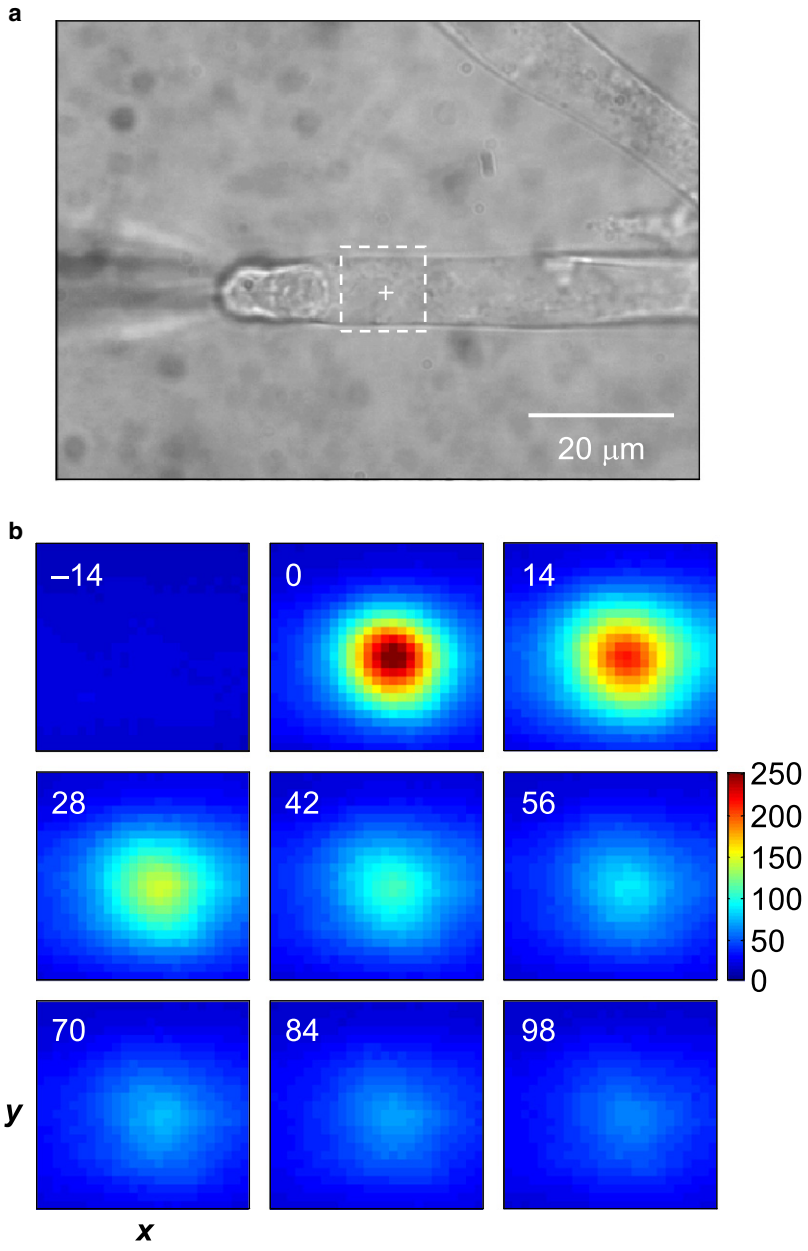

FIGURE 6 Imaging diffusion of uncaged fluorescein-dextran in the ECiS of the OHC. (*a*) Bright-field image of the OHC. The white cross and dashed square indicate the center of the uncaging spot and imaged area. (*b*) TIRFM images of the spatiotemporal distribution of uncaged fluorescein-dextran in the ECiS. Image size was 11.5 × 11.5 μm^2. The images are labeled in milliseconds as measured from the uncaging event.

from the nucleus (Fig. 6 *a*). Fig. 6 *b* shows the time course of the uncaged fluorescein dextran (10 kDa, 100 μM). The image size was 11.5 $\times$ 11.5 μm^2, image acquisition rate was 72 frames/s, and total imaging time was 4 s. Intensity profiles (Fig. 7, *a* and *b*) were taken along the axial and circumferential directions of the cell, or the *x* and *y* directions, respectively. Normalized profiles (Fig. 7, *c* and *b*) show a difference between the axial and circumferential directions, namely, wider axial profiles. This difference is due to nonuniform distance between the cell and the coverslip. Normalization with an image taken before photolysis (−14 ms; Fig. 6) abolished the difference between axial and circumferential profiles, as shown in Fig. 6, *e–h*. Both axial and circumferential profiles lack a drift of the centroid over the time course of the experiment. Only dye spreading due to the diffusion is present. The average value of the effective diffusion coefficient, D_{ECiS}, calculated for measurements in 13 cells was 14 $\pm$ 3 $\mu m^2/s$, which is significantly smaller (by a factor of 4.6) than the value measured in free solution ($P = 0.0003$, Student's *t*-test). A comparison of the diffusivity values calculated from axial and circumferential profiles (Fig. 7, *i* and *j*, respectively) showed no difference within the measurement error. Applying the depolarizing holding potential of 0 mV and +60 mV did not change the measured D_{ECiS}. To determine the transport in the AX of the OHC, the same experiments were performed using epifluorescence imaging. A bright-field image of an OHC and epifluorescence images taken during the experiments are shown in Fig. 8, *a* and *b*, respectively. Fig. 9 illustrates the determination of the effective diffusivity. The transport was purely diffusive, and the effective diffusion coefficient D_{axial} was 40 $\pm$ 11 $\mu m^2/s$ ($n = 5$). The diffusion in the AX was ~3 times faster than in the ECiS, but was slower compared to that in free solution ($P = 0.005$). The difference between D_{ECiS} and D_{axial} was statistically significant ($P = 0.006$).

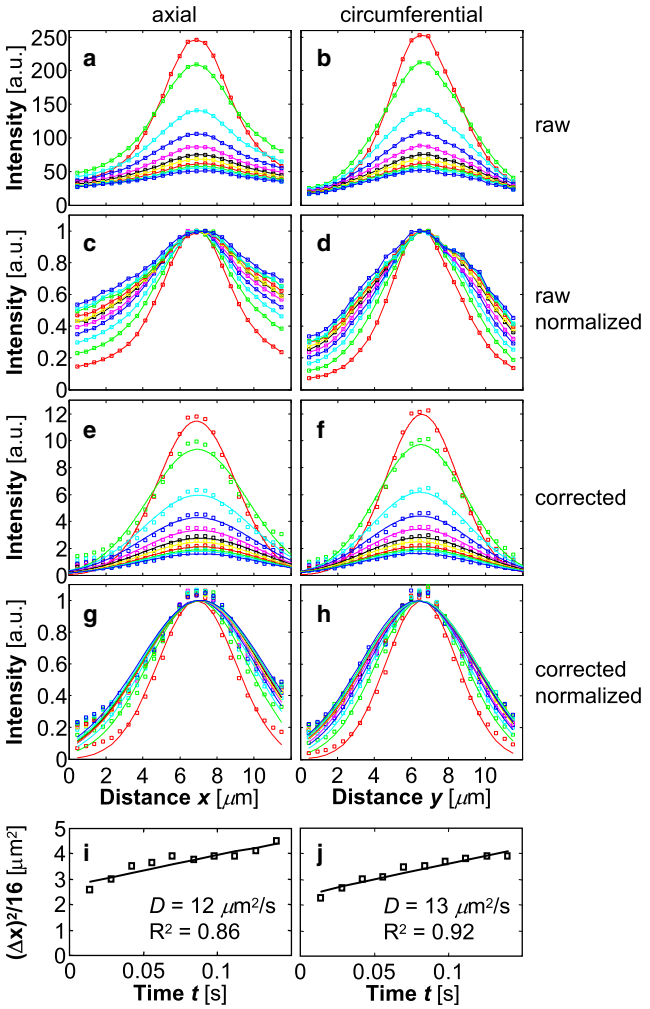

FIGURE 7 Determination of the effective diffusivity of uncaged fluorescein-dextran in the ECiS of the OHC. (*a* and *b*) Intensity profiles along the axial and circumferential directions of the cell through the center of images shown in Fig. 6 *b*. (*c* and *d*) Normalized profiles of *a* and *b*. (*e* and *f*) Corrected profiles of *a* and *b* (*squares*) were fit by Gaussians (*solid lines*). (*g* and *h*) Normalized profiles of *e* and *f*. (*i* and *j*) Squared widths of Gaussian profiles were plotted as a function of time. The slope of the line calculated by the least-square method is the effective diffusivity.

DISCUSSION

TIRFM images of OHCs, similar to the one shown in Fig. 5 *c*, revealed a specific condition of the PM, i.e., flattening of the part of the membrane that was in contact with the glass coverslip. When uncoated glass was used, the contact area between it and the OHC was very small and limited to individual patches. Therefore, the polylysine coating facilitates the cell/glass contact and may play a role in the membrane flattening. This flattening of the lateral wall may affect the thickness of the ECiS and its transport properties. Thus, our conclusion regarding the absence of the convective transport may be valid for this specific condition only. Although this flattened state of the membrane is different from the natural state, the experimental findings are still of interest because they provide insight into the structure of the lateral wall. The optical technique employed here provides information on live cells, whereas to date, all structural information has been obtained by electron microscopy. In addition, polylysine-coated glass is commonly employed for cell immobilization during electrical recordings.

The most important finding is the significant difference in the measured values of the effective diffusion coefficient for the ECiS and the AX (see Table 1). It proves the existence of the ECiS, a compartment that features significantly slower motion of molecular substances compared to the rest of the cell. The lower diffusivity ($D_{free}/D_{ECiS} = 4.6$) could be a result of several different factors, including the presence of the CL and the interaction with both the PM and the SSC. Our data do not indicate any binding of fluorophores to membranes. However, even though the observed photobleaching was not significant, it could prevent us from monitoring bound fluorophores. The smaller effective diffusivity

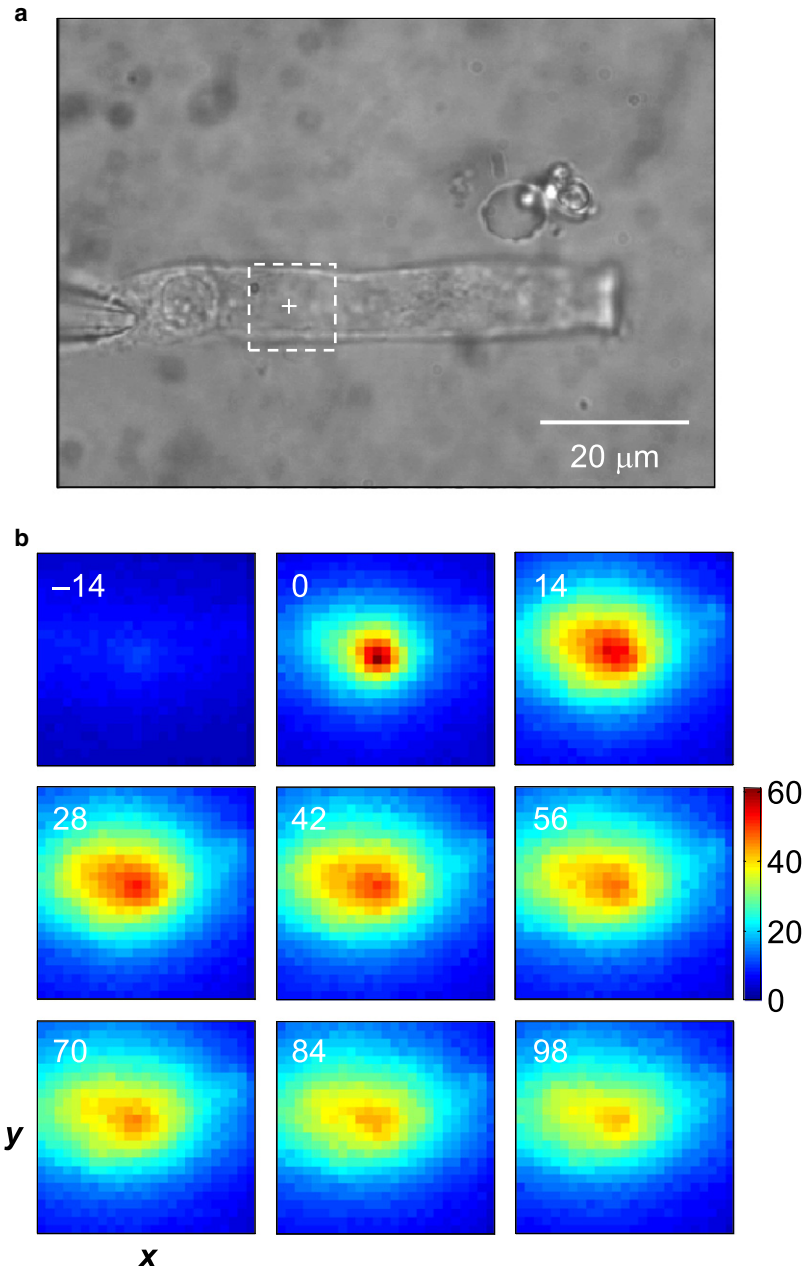

FIGURE 8 Imaging diffusion of uncaged fluorescein-dextran in the AX of the OHC. (*a*) Bright-field image of the OHC. The white cross and dashed square indicate the center of the uncaging spot and imaged area. (*b*) Epifluorescence images of the spatiotemporal distribution of uncaged fluorescein-dextran in the AX. Image size was 11.5 × 11.5 μm^2. The images are labeled in milliseconds as measured from the uncaging event.

in the AX compared with free solution ($D_{free}/D_{axial} = 1.6$) indicates that the effective viscosity of the cytoplasm is significantly higher than that of water. The diffusion was found to be isotropic in both the ECiS and the AX. Reported values for the effective viscosity of the cell cytoplasm vary significantly depending on the cell type, probe size, and other parameters. Our D_{free}/D_{axial} value may be compared with that reported for the diffusion of fluorescently labeled dextrans of different sizes in neuron cytoplasm (14). The ratio of the diffusivities in aqueous solution to neuronal cytoplasm increased with increasing size of dextrans, and was found to be 2.7 for the dextran with a hydrodynamic radius of 2 nm (close to our probe radius of 2.5 nm). The smaller ratio we observed is consistent with a lower density of solutes in the OHC cytoplasm.

The absence of drift of the fluorophores indicates that possible effects of the convection and electric field are small and undetectable on the timescale of the experiments. The sensitivity of our technique is ~1 μm/s. The possibility of the presence of convective transport of molecules was suggested based on the permeability of the PM to water, as shown in a number of studies (15–18). The hypothesis proposed by Halter et al. (19) regarding extracisternal longitudinal potential gradients and their role in experimentally observed nonlinear capacitance and electromotility was an additional motivation for our study. The absence of such

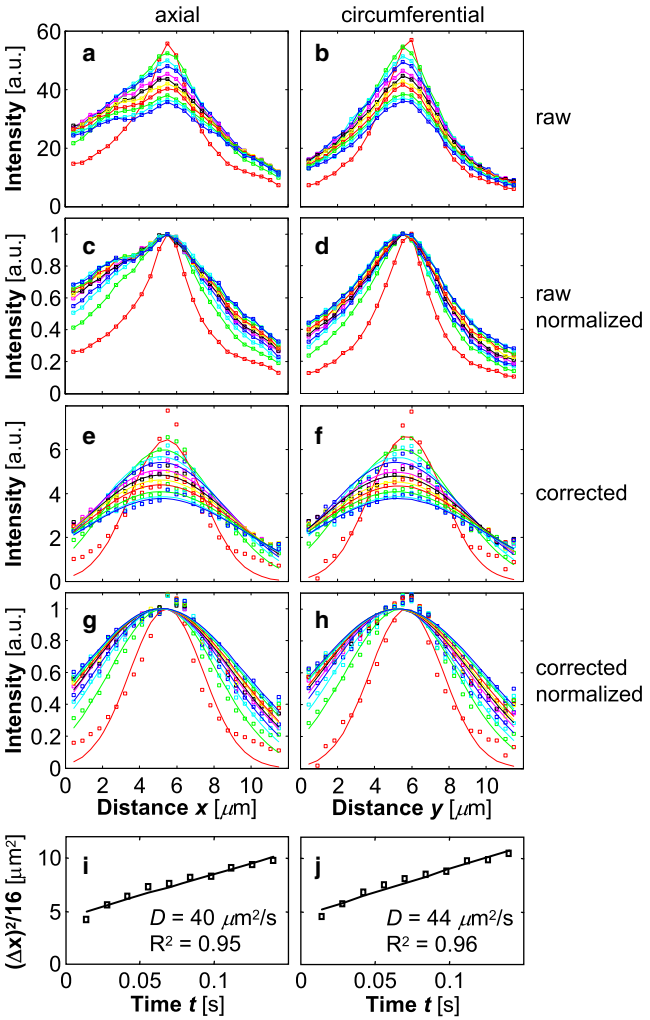

FIGURE 9 Determination of the effective diffusivity of uncaged fluorescein-dextran in the AX of the OHC. (*a* and *b*) Intensity profiles along the axial and circumferential directions of the cell through the center of images shown in Fig. 6 *b*. (*c* and *d*) Normalized profiles of *a* and *b*. (*e* and *f*) Corrected profiles of *a* and *b* (*squares*) were fit by Gaussians (*solid lines*). (*g* and *h*) Normalized profiles of *e* and *f*. (*i* and *j*) Squared widths of Gaussian profiles were plotted as a function of time. The slope of the line calculated by the least-square method is the effective diffusivity.

a drift may be explained by the above-mentioned membrane flattening or by the noncontinuous structure of the SSC. Evidence for this comes from high-resolution electron microscopy imaging, which has revealed the existence of variable numbers and degrees of fenestration of cisternal layers along the length of an individual OHC (20). At the same time, the observed fenestration could be a result of the fixation process. The limitations on image acquisition speed ($\leq$100 frames/s) prevented us from measuring the diffusivity of a low-molecular-weight fluorophore. Higher temporal resolution could be achieved by collecting fluorescence using a photomultiplier tube and measuring only within the area where uncaging occurs. The diffusion coefficient could be calculated based on the numerical fit of the temporal decay of measured fluorescence (13). This approach could provide higher detection rates, which are necessary to determine whether the structure of the ECiS impedes small anionic solute transport.

TABLE 1 Effective diffusion coefficients in $\mu m^2/s$ of fluorescein dextran (10 kDa)

Free solution	65 $\pm$ 10 ($n = 5$)
OHC, AX	40 $\pm$ 11 ($n = 5$)
OHC, ECiS	14 $\pm$ 3 ($n = 13$)

In summary, we have developed a technique to study the transport of molecules inside living cells. This was achieved by performing photolytic activation of fluorescent molecules in a small volume and tracing their spatiotemporal evolution by selective excitation within an ~100 nm thick layer near the cell/glass interface. Using this technique, we were able to show that the transport of fluorescein dextran molecules in the ECiS of the OHC is diffusive. Compared with the AX and free solution, the effective diffusion coefficient in the ECiS is reduced by a factor of ~2.9 and ~4.6, respectively. The molecular drift due to convection or electric field is small and, if present, below the sensitivity of our technique. The diffusion in the ECiS is isotropic and does not change with depolarization of the OHC. The effective diffusivity in the AX is reduced compared with that in free solution.

We thank Brenda Farrell for support with the experiments and valuable suggestions.

This work was supported by grants from the National Institutes of Health and the National Science Foundation to P.S. and W.E.B.

REFERENCES

1. Brownell, W. E., C. R. Bader, D. Bertrand, and Y. Deribaupierre. 1985. Evoked mechanical responses of isolated cochlear outer hair-cells. *Science*. 227:194–196.
2. Liberman, M. C., J. G. Gao, D. Z. Z. He, X. D. Wu, S. P. Jia, et al. 2002. Prestin is required for electromotility of the outer hair cell and for the cochlear amplifier. *Nature*. 419:300–304.
3. Brownell, W. E., and A. S. Popel. 1998. Electrical and mechanical anatomy of the outer hair cell. *In* Psychophysical and Physiological Advances in Hearing. A. R. Palmer, A. Rees, A. Q. Summerfield, and R. Meddis, editors. Whurr Publishers, London. 89–96.
4. Brownell, W. E. 1990. Outer hair cell electromotility and otoacoustic emissions. *Ear Hear*. 11:82–92.
5. Ratnanather, J. T., A. S. Popel, and W. E. Brownell. 2000. An analysis of the hydraulic conductivity of the extracisternal spade of the cochlear outer hair cell. *J. Math. Biol*. 40:372–382.
6. Chary, S. R., and R. K. Jain. 1989. Direct measurement of interstitial convection and diffusion of albumin in normal and neoplastic tissues by fluorescence photobleaching. *Proc. Natl. Acad. Sci. USA*. 86: 5385–5389.
7. Ramanujan, S., A. Pluen, T. D. Mckee, E. B. Brown, Y. Boucher, et al. 2002. Diffusion and convection in collagen gels: implications for transport in the tumor interstitium. *Biophys. J*. 83:1650–1660.
8. Swaminathan, R., S. Bicknese, N. Periasamy, and A. S. Verkman. 1996. Cytoplasmic viscosity near the cell plasma membrane: translational diffusion of a small fluorescent solute measured by total internal reflection-fluorescence photobleaching recovery. *Biophys. J*. 71:1140–1151.

9. Kaplan, J. H., and A. P. Somlyo. 1989. Flash-photolysis of caged compounds—new tools for cellular physiology. *Trends Neurosci.* 12:54–59.

10. Nerbonne, J. M. 1996. Caged compounds: tools for illuminating neuronal responses and connections. *Curr. Opin. Neurobiol.* 6:379–386.

11. Thompson, N. L., and B. C. Lagerholm. 1997. Total internal reflection fluorescence: applications in cellular biophysics. *Curr. Opin. Biotechnol.* 8:58–64.

12. Toomre, D., and D. J. Manstein. 2001. Lighting up the cell surface with evanescent wave microscopy. *Trends Cell Biol.* 11:298–303.

13. Xia, P., P. M. Bungay, C. C. Gibson, O. N. Kovbasnjuk, and K. R. Spring. 1998. Diffusion coefficients in the lateral intercellular spaces of Madin-Darby canine kidney cell epithelium determined with caged compounds. *Biophys. J.* 74:3302–3312.

14. Popov, S., and M. M. Poo. 1992. Diffusional transport of macromolecules in developing nerve processes. *J. Neurosci.* 12:77–85.

15. Belyantseva, I. A., G. I. Frolenkov, J. B. Wade, F. Mammano, and B. Kachar. 2000. Water permeability of cochlear outer hair cells: characterization and relationship to electromotility. *J. Neurosci.* 20:8996–9003.

16. Chertoff, M. E., and W. E. Brownell. 1994. Characterization of cochlear outer hair cell turgor. *Am. J. Physiol.* 266:C467–C479.

17. Morimoto, N., R. M. Raphael, A. Nygren, and W. E. Brownell. 2002. Excess plasma membrane and effects of ionic amphipaths on mechanics of outer hair cell lateral wall. *Am. J. Physiol. Cell Physiol.* 282:C1076–C1086.

18. Ratnanather, J. T., M. Zhi, W. E. Brownell, and A. S. Popel. 1996. Measurements and a model of the outer hair cell hydraulic conductivity. *Hear. Res.* 96:33–40.

19. Halter, J. A., R. P. Kruger, M. J. Yium, and W. E. Brownell. 1997. The influence of the subsurface cisterna on the electrical properties of the outer hair cell. *Neuroreport.* 8:2517–2521.

20. Furness, D. N., and C. M. Hackney. 1990. Comparative ultrastructure of subsurface cisternae in inner and outer hair-cells of the guinea-pig cochlea. *Eur. Arch. Otorhinolaryngol.* 247:12–15.